Nano Research
2022, 15(9): 8555–8563

ISSN 1998-0124 CN 11-5974/O4
https://doi.org/10.1007/s12274-022-4417-0

Research Article

AgAuSe quantum dots with absolute photoluminescence quantum yield of 87.2%: The effect of capping ligand chain length

Ziqiang Sun[1,2], Cheng Liu[3], Hongchao Yang[2] (✉), Xiaohu Yang[2], Yejun Zhang[2], Hongzhen Lin[2], Youyong Li[3], and Qiangbin Wang[1,2] (✉)

[1] *School of Nano-Tech and Nano-Bionics, University of Science and Technology of China, Hefei 230026, China*
[2] *CAS Key Laboratory of Nano-Bio Interface, Division of Nanobiomedicine and i-Lab, Suzhou Institute of Nano-Tech and Nano-Bionics, Chinese Academy of Sciences, Suzhou 215123, China*
[3] *Institute of Functional Nano & Soft Materials (FUNSOM), Jiangsu Key Laboratory for Carbon-Based Functional Materials & Devices, Soochow University, Suzhou 215123, China*

Received: 11 April 2022 / **Accepted:** 11 April 2022

ABSTRACT

Surface ligands of colloidal quantum dots (QDs) have a profound influence on their surface states, which has been verified in the studies of the effect of ligand head groups on the photoluminescence (PL) properties of QDs. However, the investigation of the ligand chain length is limited. Here, we systematically explored the effect of chain length on the Ag_2Se QDs by selecting three ligands, 1-octanethiol (OTT), 1-dodecanethiol (DDT), and 1-hexadecanethiol (HDT), with diverse chain lengths. We found that the PL intensity of Ag_2Se QDs increased with the decrease of the ligand chain length due to the enhanced passivation of surface defects emerging from the robust QD-ligand interface binding affinity and the weaker hydrophobic chain–chain interaction. Subsequently, AgAuSe QDs terminated with OTT were obtained by alloying parent OTT-Ag_2Se QDs with Au precursor with a record absolute PL quantum yield (PLQY) of 87.2% at 970 nm, facilitating ultrasensitive *in vivo* angiography imaging in a nude mouse model. We expect that our finding of the important role of the ligand chain length on the optical properties of QDs will be suggestive to the design and synthesis of high-quality QDs, and also look forward to the clinical applications of the ultra-bright AgAuSe QDs.

KEYWORDS

quantum dots, surface ligand, ligand chain length, photoluminescence quantum yield, bioimaging

1 Introduction

Surface ligands are an indispensable component of colloidal semiconductor quantum dots (QDs), which play important roles in determining their physico-chemical properties [1–5]. Generally, QDs have been synthesized in a solution containing hydrophobic precursor ligands with an anchoring head group (e.g., thiols, amines, carboxylate, and phosphines) tethered to the QD surface and an aliphatic chain (C_8-C_{18}) away from it [6–9]. These ligand molecules adhere to QD surface and form a capping layer, which controls the nucleation and growth kinetics during synthesis process, isolates the particle from their environment in maintaining colloidal stability, and impacts their solubility in media [6, 10–12]. Besides, ligands also have a substantial influence on the optical and electronic properties of QDs, since they can saturate the dangling bonds by coordination with surface atoms and passivate surface defects to eliminate the mid-gap trap states [3, 13–16].

Nevertheless, the adsorption/desorption equilibrium of the capped ligands anchored to the QD surface in solution is highly dynamic and susceptible to multitudinous factors, including QD-ligand interface binding affinity, particle curvature, concentration and polarity of solvents, etc [17, 18]. Once perturbed, the ligands may shed from the QD surface to expose the trap sites and promote the nonradiative relaxation, resulting the decrease of the photoluminescence quantum yield (PLQY) of QDs [18, 19]. To understand the origin of the surface ligands effect on the optical properties of QDs, extensive efforts have been taken to investigate the influence of ligand head groups towards QDs, in which the interactions between binding groups and the surface atoms are viewed as a predominant reason for the change of PL properties [3, 20–22]. In addition, the branched structures, functional groups, and chain lengths of ligand molecules also have significant impact on the optical properties of QDs [5, 23, 24]. For example, ligands with branched chains usually led to a lower surface ligand coverage of QDs because of their larger steric hindrance, unfavorable to the PL properties. Also, ligand chain modified with electron withdrawing/donating groups could regulate the binding states by altering the electron density of head groups, placing significant impacts on the trap states and PL properties [23]. However, the effect of the ligand chain length on the PL properties of QDs is not yet clear till now. Only a handful reports investigated the ligand-exchange thermodynamics and described the chain length-dependent interchain interactions of QDs [25, 26]. Accordingly, an elaborated study to reveal the effect of ligand chain length on the optical properties of QDs is essential.

Address correspondence to Hongchao Yang, hcyang2014@sinano.ac.cn; Qiangbin Wang, qbwang2008@sinano.ac.cn

Herein, three typical straight-chain thiol ligands of various chain length (1-octanethiol (OTT), n = 7; 1-dodecanethiol (DDT), n = 11; and 1-hexadecanethiol (HDT), n = 15) were selected as coordinating ligands to probe the impact of ligand chain length on the optical properties of Ag_2Se QDs. With the decrease of the ligand chain length, the PL intensity of Ag_2Se QDs exhibited an increasing tendency, and OTT was found as the capping ligand to synthesize Ag_2Se QDs with the highest PL intensity. Experimental results and theoretical calculations revealed that the enhancement of PL intensity upon the decrease of ligand chain length was predominantly ascribed to the better passivation of surface defects driving from its stronger interfacial binding affinity. In addition, the disordered surface conformation of OTT-Ag_2Se verified by the sum frequency generation (SFG) measurement is also conducive to its PL enhancement, because the shorter alkyl chain length of OTT induced weaker hydrophobic chain–chain interaction compared with DDT and HDT, resulting denser coverage of OTT on the QD surface and less surface trap states. Subsequently, the OTT-AgAuSe QDs were obtained by alloying Ag_2Se QDs with Au precursor, which possessed spectacular absolute PLQY of 87.2% and 86.3% at 970 and 1,045 nm, respectively. Further, PEGylated OTT-AgAuSe enabled *in vivo* angiography imaging at an ultra-low dosage of 185 μg·kg^{-1} under an ultra-low 808 nm laser excitation intensity of 2 mW·cm^{-2}, which was of great significance for the potential clinical translation of AgAuSe QDs avoiding the biosafety concerns.

2 Experimental section

2.1 Materials and equipment used in measurements

AgAc (99%), Se powder (metal basis, 99.9999%), and $HAuCl_4{\cdot}3H_2O$ (99.99%) were purchased from Alfa Aesar. 1-octadecene (ODE), OTT, DDT (98%), HDT, tri-n-octylphosphine (TOP, $C_{24}H_{51}P$, 97%), oleylamine (OAM, $C_{18}H_{37}N$, 85%), chloroform-*d* ($CDCl_3$), and tetrahydrofuran (THF, C_4H_8O) were purchased from Acros. Indocyanine green (ICG) was purchased from Aladdin. DSPE-mPEG2000 was purchased from Nanocs Inc. (USA). All these reagents were of analytical grade and used without further purification. The morphologies of QDs were examined through a Tecnai G2 F20 S-Twin transmission electron microscopy (TEM) at an acceleration of 200 kV. The energy-dispersive X-ray (EDX) elemental mappings were recorded on JEM ARM200F. Powder X-ray diffraction (PXRD) patterns were recorded on a Bruker D8 Advance powder X-ray diffractometer, using Cu-Kα radiation (λ = 1.54056 Å). Fourier transform infrared spectroscopy (FTIR) experiments were performed on the equipment of Nicolet 6700. X-ray photoelectron spectroscopy (XPS) experiments under ultrahigh vacuum (10^{-8}–10^{-9} Torr) were performed in an ESCALAB 250 XI system with a monochromatic X-ray source (Al Kalfa line of 1,486.6 eV energy and 350 W, ultraviolet photoelectron spectroscopy (UPS) measurements were performed on an electron spectrometer using the monochromatic HeI radiation 21.22 eV). The thermogravimetric analysis (TGA) was carried out by the equipment of Q500. Nuclear magnetic resonance (NMR) data were collected by a Bruker Avance III HD 400 MHz apparatus. The absorption spectra were recorded with Biomate 160 ultraviolet–visible–near infrared ray (UV–vis–NIR) spectrophotometer (ThermoFisher Scientific, USA). The NIR fluorescence spectra were executed on Applied NanoFluorescence Spectrometer (USA) at room temperature, applying an excitation laser source of 785 nm. The SFG measurement was carried out by using the picosecond SFG spectrometer laser system built by EKSPLA, using a copropagating configuration. The IR pulses around 2,750–3,000 cm^{-1} were about 25 ps at 50 Hz. The incident angle is 55° for the IR beam. The absolute PLQY and PL time decays were measured and recorded with a calibrated spectrofluorometer (Edinburgh Instruments, FLS1000) equipped with an integrating sphere. The second near-infrared (NIR-II) fluorescence imaging was performed with small animal imaging system (Suzhou NIR-Optics, China) equipped with 900 and 1,000 nm long-pass filters.

2.2 Synthesis of Ag_2Se QDs capped with diverse thiol ligands

Firstly, 5 mmol Se (0.395 g) was dissolved in 10 mL TOP under continuous stirring for 3 h and O_2-proof storage to prevent oxidation, forming the Se precursor (TOP-Se). Then, taking the synthesis of 4.5 nm OTT-Ag_2Se QDs for example, 0.0334 g AgAc (0.2 mmol), 2.0 g OTT, and 8.0 mL ODE were loaded in a 100 mL three-neck flask and heated to 110 °C under N_2 flow to obtain a clear solution. Subsequently, the above mixture was heated to 160 °C . Then, 0.1 mL fresh TOP-Se (0.05 mmol) solution was swiftly injected into the reaction mixture under vigorous stirring and remained this temperature for 1.5 h. The products were mixed with ethanol (C_2H_6O) and precipitated through centrifugation. The precipitate was dispersed in chloroform ($CHCl_3$) for further use. In terms of synthesis of Ag_2Se QDs coated with DDT or HDT, the reactions were performed under identical conditions (the molar ratio of Ag/Se, injection temperature, and purified times), except for the terminated ligands. In addition, the size of Ag_2Se QDs could be adjusted by prolonging or shortening the reaction time.

2.3 Synthesis of Ag_2Se QDs capped with OAM

In a typical synthesis of Ag_2Se QDs capped with OAM, 0.0334 g AgAc (0.2 mmol), 2.0 mL OAM, and 8.0 mL ODE were loaded in a 100 mL three-neck flask and heated to 110 °C under N_2 flow to obtain a clear solution. Subsequently, the above mixture was heated to 120 °C and 0.1 mL fresh TOP-Se (0.05 mmol) solution was swiftly injected into the reaction mixture under vigorous stirring and remained this temperature for 0.5 h. The products were mixed with ethanol and precipitated through centrifugation. The precipitate was dispersed in chloroform-*d* for further use.

2.4 Synthesis of AgAuSe QDs

Firstly, $HAuCl_4{\cdot}3H_2O$ (1 mmol) was dissolved in 10 mL chloroform/OAM mixed solution to form the Au precursor. Then, 0.1 mL Au precursor solution was swiftly added into the solution contained Ag_2Se QDs (0.01 mmol) and reacted for 6 h. The final products were purified with ethanol through centrifugation. In detail, as the Au precursor was incorporated into as-prepared Ag_2Se QDs, the atomic ratio of Au/Ag monitored by inductively coupled plasma optical emission spectrometry (ICP-OES) increased continuously until it was approximated to 1:1, and the alloyed products termed as AgAuSe QDs were obtained.

2.5 Preparation of PEGylated AgAuSe QDs

To make these QDs hydrophilic, we cladded the surface of nanoparticles with a monolayer of functional phospholipids. 1 mg AgAuSe QDs and 10 mg DSPE-mPEG2000 were dispersed in THF solution. Then, the mixture solution was titrated into 10 mL deionized water under the condition of ultrasound (30 W) for 5 min, followed by ultrafiltration three times (3,000 rpm·min^{-1}).

2.6 TGA experiments and the calculation of ligand density

The TGA experiments were carried out by the equipment of Q500. The temperature range was set as 25–600 °C , the heating

rate was 10 °C·min^{-1}, and the whole process was carried out in N_2 environment. The calculation of ligand density of Ag_2Se QDs was according to the results of TGA analysis. As shown in Fig. S4 in the Electronic Supplementary Material (ESM), taking the 4.5 nm OTT capped Ag_2Se QDs (r = 2.25 nm and $\rho_{crystal}$ = 8 g·cm^{-3}) for example, the detail process is as followed

$$W_{crystal} = \rho_{crystal} V_{crystal} = 8(4\pi r^3/3)$$

where r and $\rho_{crystal}$ represent the radius of QD and the crystal density of cubic Ag_2Se QDs, respectively. $W_{crystal}$ and $V_{crystal}$ represent the weight and volume of QD, repectively.

According to the TGA results, the weight of OTT (W_{OTT}) is 19.5% of total weight

$$W_{OTT} = W_{crystal} \times 19.5/80.5$$

where W_{OTT} represents the weight of ligand (OTT).

Since the molecular weight of OTT is 146 g·mol^{-1}, the number of OTT ligand (N_{OTT}) is calculated to be

$$N_{OTT} = N_A \times (W_{OTT}/146)$$

where N_{OTT} represents the number of ligand (OTT). N_A is Avogadro constant (6.022×10^{23} mol^{-1}).

Ligand density ρ_{OTT} of OTT-Ag_2Se is calculated to be $\rho_{OTT} = N_{OTT} \cdot (4\pi r^2)^{-1} = 5.99$ nm^{-2}.

Similarly, the ligand densities of Ag_2Se capped with DDT and HDT are calculated to be $\rho_{DTT} = 5.92$ nm^{-2} and $\rho_{HDT} = 5.78$ nm^{-2}.

2.7 Density functional theory (DFT) calculations

All the DFT calculations were carried out by DMol^3 program [27]. The generalized gradient approximation with Perdew–Burke–Ernzerhof (GGA-PBE) functional was used to describe the effects of electronic exchange and correlation [28]. The convergence tolerance values for energy, force, and displacement were specified as 1×10^{-5} Ha, 2×10^{-3} Ha·Å^{-1}, and 5×10^{-3} Å^{-1}, respectively. To investigate the performance of ligands on the Ag_2Se surface, the adsorption energies (E_{ads}) of OTT, DDT, and HDT on the surface of Ag-rich Ag_2Se(200) surface have been calculated as follows

$$E_{ads} = E_{base} + E_{mol} - E_{total}$$

where E_{total} and E_{base} represent the total energy of Ag_2Se surface with and without the adsorption of ligands. E_{mol} is the energy of these three ligands in free states.

2.8 NMR experiment and ligand exchange experiments

To acquire the relative magnitude of binding affinity between QDs and diverse thiol ligands, we calculated the amount of thiol ligands adhered on the surface of Ag_2Se QDs after ligand exchange reactions with OAM-Ag_2Se QDs. That is, the OAM capped Ag_2Se QDs were selected as raw materials and underwent the ligand exchange processes with diverse thiol ligands (OTT, DDT, and HDT), respectively. As shown in Fig. S9 in the ESM, firstly, the proton peak signals of free and bound ligand (OAM and thiol ligands) were tested (OAM, DTT, OAM-Ag_2Se QDs, and OTT-Ag_2Se QDs solution was dried under Ar flow, and then re-dissolved in chloroform-*d*). Then, the target signal peak information after ligand exchange was extracted separately. 50 μL ligand solutions (OTT, DDT, and HDT) were titrated into chloroform-*d* solution contained OAM-Ag_2Se (0.2 mg·mL^{-1}, 550 μL), respectively, and reacted adequately before test. Due to the differences in chemical environment, the bound ligands exhibited distinct chemical shifts versus the unbound ligands. As thus, the proton peak of $-CH_2-$ adjacent to sulfhydryl group moved from 2.7 to 3.2 ppm. As shown in Fig. S10 in the ESM, according to the peak areas corresponding to the bound and free ligands, and the total number of thiol ligands added, the number of bound thiol ligands could be quantified through the equation as followed

$$N_{bound} = (S_{bound}/S_{bound} + S_{unbound}) \times N_{total}$$

where N_{bound} and N_{total} represent the number of thiol ligand bound on the QD surface and total thiol ligand added. S_{bound} and $S_{unbound}$ represent the peak areas corresponding to the bound and free ligands in ^{1}H NMR spectra.

Taking OAM-Ag_2Se treated with OTT for example, N_{bound} = (1/12.53) × (0.843 × 50/146) = 0.023 mmol. Similarly, the bound ligand numbers were calculated, 0.017 mmol for DTT and 0.014 mmol for HDT.

2.9 PLQY and lifetime measurements

The absolute PLQY and PL time decays were measured and recorded with a calibrated spectrofluorometer (Edinburgh Instruments, FLS1000) equipped with an integrating sphere. A Xe lamp was used as the excitation source, filtered with a long-pass filter (610 nm) and a monochromator (wavelength: 750 nm and bandwidth: 20 nm). The PLQY of AgAuSe QDs was calculated by dividing the total number of emitted photons in the 800–1,200 nm range by the total number of absorbed photons at 750 nm.

2.10 *In vivo* fluorescence imaging of mice

In vivo NIR-II fluorescence imaging was carried out by using NIR-II *in vivo* imaging system (Series II 900/1700, Suzhou NIR Optics Technologies Co., Ltd., China). A zoom lens assembly (Navitar 6000) was used to achieve high spatial resolution. The nude mice were injected intravenously with PEGylated AgAuSe QDs and ICG, respectively. 2 L·min^{-1} O_2 flow with 2% isoflurane ($C_{14}HF_{29}O_4$) was used for anesthesia of the mice during injection and imaging. The mice were imaged using NIR-II fluorescence imaging system. The excitation light was provided by an 808 nm diode laser with a power density at the imaging plane of 2 mW·cm^{-2}. The 1,000 nm long-pass filter was employed for collecting the fluorescent signal.

3 Results and discussion

3.1 The characterization of Ag_2Se QDs capped with diverse thiol ligands

According to the principle of hard and soft acids and bases (HSAB), sulfhydryl ligand as one sort of soft Lewis bases, has stronger binding strength with Ag(I) than other ligands like $-NH_2$ and –COOH, which was avail to balance the nucleation and growth of Ag_2Se QDs [29, 30]. Thereby, we prepared three types of Ag_2Se QDs terminated with various chain length straight-chain thiol ligands (OTT, DDT, and HDT) to investigate the effect of chain length on their optical properties. As demonstrated in Fig. 1(a), Ag_2Se QDs were synthesized with three kinds of ligands (OTT, DDT, or HDT) under identical conditions, respectively (see Experimental section for details).

Figures 1(b)–1(d) exhibited TEM images of Ag_2Se QDs capped with OTT, DDT and HDT, respectively, showing the monodisperse spherical structure with similar size distributions of 4.53 ± 0.29 nm (OTT-Ag_2Se), 4.46 ± 0.36 nm (DDT-Ag_2Se), and 4.49 ± 0.54 nm (HDT-Ag_2Se) (Fig. S1 in the ESM). The high-resolution TEM (HRTEM) images confirmed that these Ag_2Se QDs were single crystalline structures with well-developed lattice fringes. The interplanar spacing of 0.25 nm was assigned to the lattice distance of (200) facet of cubic Ag_2Se QDs. PXRD patterns

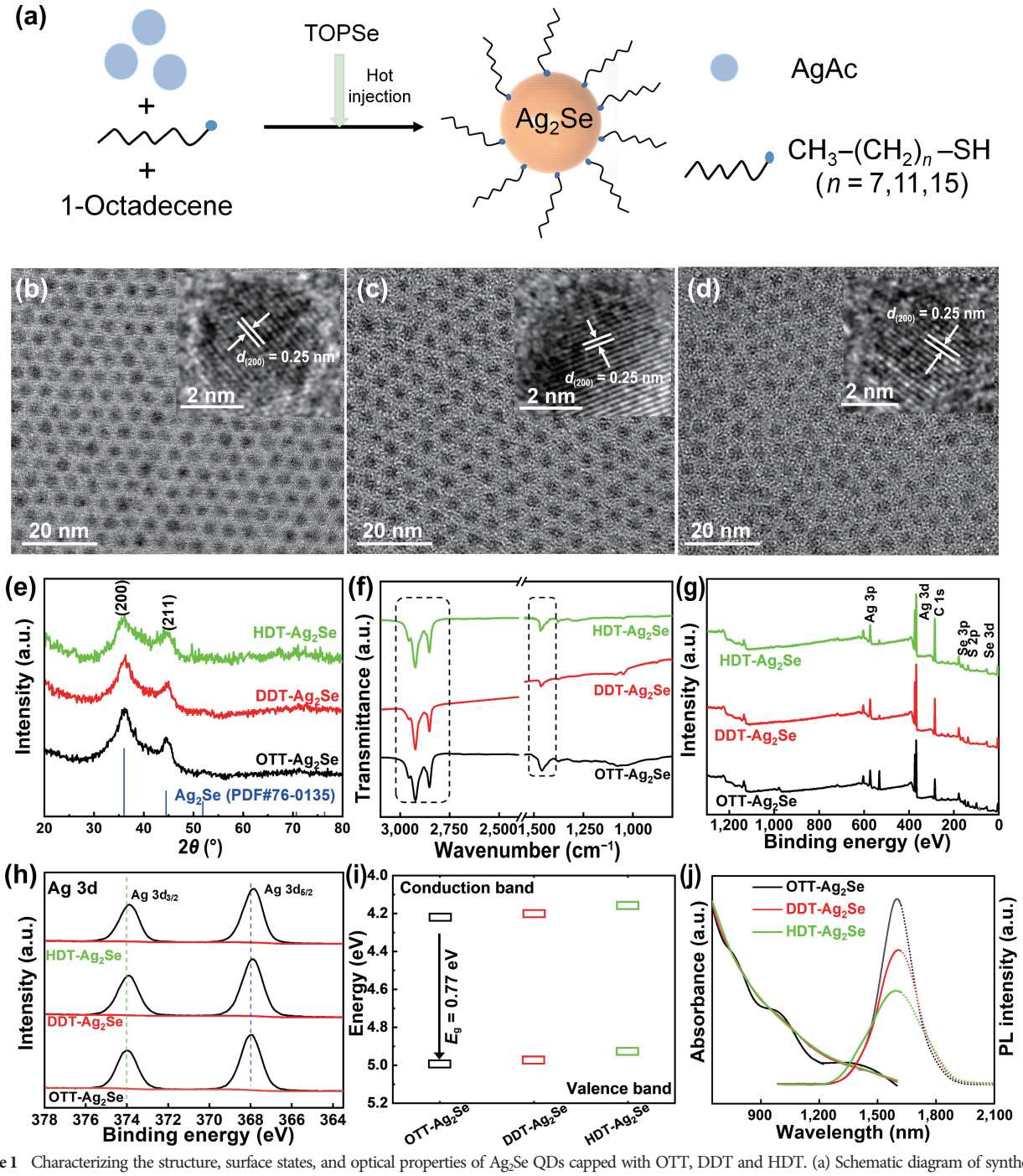

Figure 1 Characterizing the structure, surface states, and optical properties of Ag_2Se QDs capped with OTT, DDT and HDT. (a) Schematic diagram of synthesis of Ag_2Se QDs with OTT, DDT, and HDT ligands. TEM images of (b) OTT-Ag_2Se, (c) DDT-Ag_2Se, and (d) HDT-Ag_2Se QDs. (e) PXRD patterns, (f) FTIR spectra, (g) XPS survey spectra, (h) high-resolution XPS of Ag 3d region, and (i) bandgaps of OTT-, DDT- and HDT-capped Ag_2Se QDs. The bandgap in (i) was determined from the Tauc plot. (j) UV–vis–NIR absorption spectra and PL spectra of the as-prepared Ag_2Se QDs with the same atomic concentration (since the response range of PL spectrometer was < 1,620 nm, the PL emission above 1,620 nm was fitted with a dotted line). The excitation wavelength of PL spectra was 785 nm.

in Fig. 1(e) revealed these as-prepared Ag_2Se QDs had a body-centered cubic (bcc) phase structure (JCPDS No. 76-0135), which was consisted with the results of HRTEM. In addition, as shown in FTIR results (Fig. 1(f)), the peaks of $-CH_3$ and $-CH_2-$ in alkyl chain existed (2,840–2,950 and 1,460 cm^{-1}), while no characteristic peak of free thiols (2,490 cm^{-1}) was observed in these samples, indicating that these native thiol ligands were successfully anchored on the QD surface.

Furthermore, XPS measurement was adopted to investigate the surface chemical states and binding strength of these Ag_2Se QDs. As depicted in Fig. 1(g), the XPS analysis indicated that these samples were constituted of elements of Ag, Se, and S. In high-resolution XPS spectra, no significant changes were discerned in the regions of S 2p and Se 3d (Fig. S2 in the ESM), while the two Ag 3d signal peaks at 368.0 (Ag $3d_{5/2}$) and 374.0 eV (Ag $3d_{3/2}$) of Ag_2Se QDs were slightly shifted toward higher binding energy as the chain length of ligands decreased (Fig. 1(h)). Quantitative analyses of the XPS results exhibited all as-prepared QDs had a similar Ag/Se ratio of 2.4/1, revealing the Ag-rich nature (Fig. S3 in the ESM). However, the OTT-Ag_2Se QDs possessed a slightly higher proportion of S atom in comparison with DDT- and HDT-capped Ag_2Se QDs, which was subsequently verified by TGA and derived from higher ligand density (Fig. S4 in the ESM). Further, UPS measurement was performed to elucidate the influence of ligands on the state of valance electrons in these samples (Fig. S5 in the ESM). As presented in Fig. 1(i), the energy level positions of

valence band and conductor band in Ag_2Se QDs exhibited a subtle rise on account of the change of dipole moment upon increasing the carbon chain from 8 to 12 and 16 [31]. Taken together, the XPS and UPS analyses indicated the sulfhydryl ligands of various chain lengths played an important role on the surface states of Ag_2Se QDs.

Subsequently, we measured the optical properties including absorptions and emissions of these Ag_2Se QDs at room temperature. As depicted in Fig. 1(j), the absorption spectrum of 4.5 nm OTT-Ag_2Se exhibited obvious characteristic absorption peaks at 780, 1,000, and 1,400 nm in comparison to the DDT-Ag_2Se and HDT-Ag_2Se QDs. It might be ascribed to the increased electron localization for OTT-Ag_2Se QDs. In addition, the PL spectra presented the emission peaks of all as-prepared Ag_2Se QDs were centered at 1,600 nm. Interestingly, an increase in PL intensity was observed as the ligand chain length decreased under the same atomic concentration of Ag_2Se QDs, accompanying with the narrowing-down of the full width at half-maximum (FWHM) of PL spectra, which could be reasoned to the decreased size distribution or the drop of defect density (Fig. S6 in the ESM). Importantly, the improvement of PL intensity induced by short chain length was also observed with another set of Ag_2Se QDs emitted at 1,270 nm with OTT, DDT, and HDT as capping ligands (Fig. S7 in the ESM), in which OTT-capped Ag_2Se QDs presented the strongest PL intensity.

3.2 Mechanism analysis of the ligand chain length effect on the optical properties of Ag_2Se QDs

To fully understand the intrinsic mechanism why the QD-ligand interface changes the PL intensity in Ag_2Se QDs, first-principles calculation based on DFT was executed. In light of the ligand molecular structures, compared with DDT and HDT, OTT with shorter electron donating alkyl chain resulted in smaller highest occupied molecular orbital-lowest unoccupied molecular orbital (HOMO-LUMO) gap, which corresponded to its softer and more polarizable binding head (Fig. 2(a)) [23]. Based on the concept of HSAB, a stronger bond between Ag and OTT was formed by electrostatic interaction [1, 30]. Subsequently, we established an adsorption model to calculate the QD-ligand interface E_{ads} (Fig. S8 in the ESM) [32]. Guided by *ab initio* calculations, the exposed Ag-rich (200) crystal facet of Ag_2Se QDs was selected as active site for the adsorption of ligand. Taking OTT-Ag_2Se as example, the S moiety in ligand was inclined to bind with Ag site rather than Se site because of the lower E_{ads}, forming S–Ag_3 bond (Fig. 2(b)). Figure 2(c) presented the optimized configurations and the corresponded ligand-QD E_{ads} in OTT-, DDT-, and HDT-capped Ag_2Se QDs, respectively. The largest negative values of E_{ads} between QD and OTT certified a more thermodynamically stable anchoring condition of OTT-Ag_2Se QDs, which agreed with the explanation of HSAB theory. Moreover, we performed the ligand exchange experiments monitored by quantitative ^{1}H NMR to prove the DFT simulation results (see Experimental section for details). The ^{1}H NMR results illustrated that more OTT ligand molecules were bound on the surface of Ag_2Se QDs than those in DDT and HDT cases, confirming the robust binding affinity between Ag_2Se QDs and OTT molecules (Fig. 2(d) and Figs. S9 and S10 in the ESM). Taking account of the DFT calculations and ^{1}H NMR results as well as the TGA results, we speculated that the enhanced PL intensity of OTT-Ag_2Se QDs was ascribed to the strong interfacial interaction between QD and OTT ligand, benefiting the well-protected surface state and the obstructed nonradiative relaxation.

Previous studies have reported that the ordering of ligands on the QD surface was another factor in affecting the luminescence of QDs, in which the ordered pattern of ligands was deemed to have negative influence on the optical properties of QDs [24]. A possible explanation was that the change in ligand conformation affected by the alkyl chain length-dependent interaction would alter the QD-ligand binding angle onto the QD surface and impact the surface trap states [24]. Therefore, we utilized the SFG

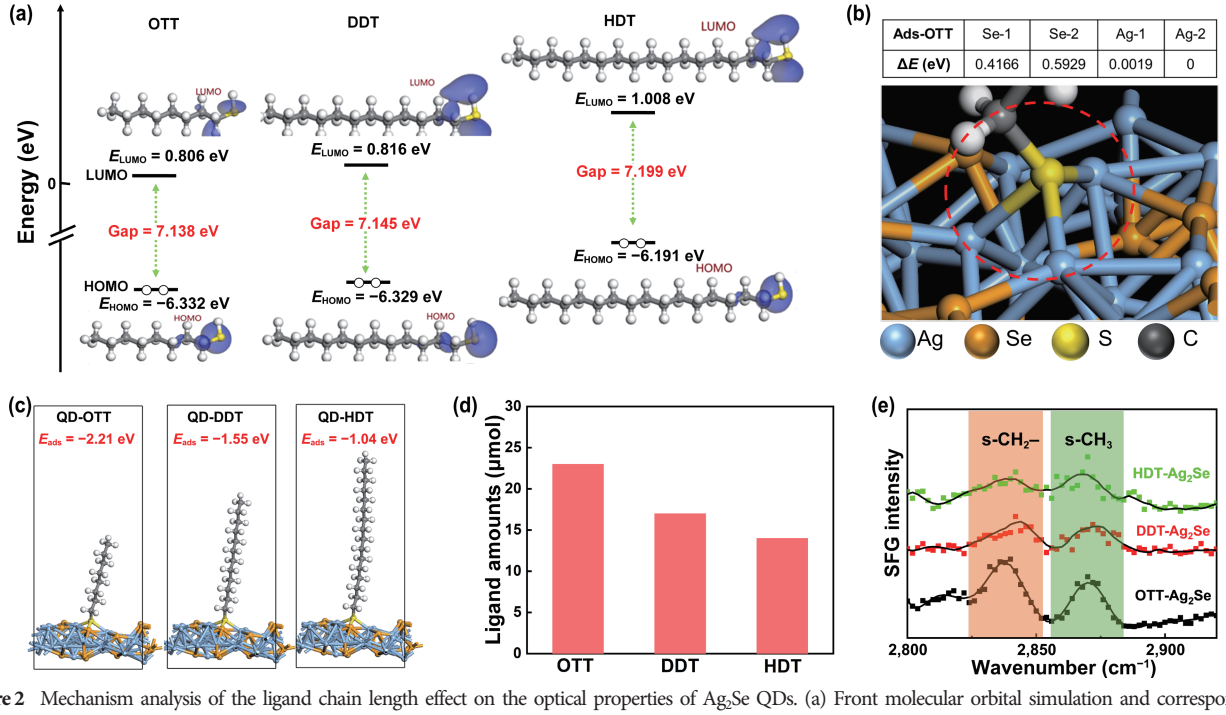

Figure 2 Mechanism analysis of the ligand chain length effect on the optical properties of Ag_2Se QDs. (a) Front molecular orbital simulation and corresponding energy level diagram of OTT, DDT, and HDT. (b) Taking OTT-capped Ag_2Se QDs as an example, the preferential bonding mode (S–Ag_3) between thiol ligands and QDs was calculated by comparing the absorption energies between S moiety in ligand and active site on the Ag_2Se surface. (c) Optimized adsorption configurations and the corresponding E_{ads} of a single OTT, DDT, or HDT molecule capped on Ag_2Se QDs surface. (d) The numbers of OTT, DDT, and HDT capped on Ag_2Se QDs surface, which were calculated from the results of ^{1}H NMR measurement. (e) The SFG results of OTT-, DDT-, and HDT-capped Ag_2Se QDs. The ratio of s-CH_3/s–CH_2– was used to analyze the order degree of different ligand patterning on Ag_2Se QDs surface.

measurement to inspect the order degree of the ligand pattern on the QD surface. As described in Fig. 2(e), two characteristic aliphatic tail structure vibrations located at 2,870 and 2,830 cm^{-1} were observed, which represented the methyl end group (s–CH_3) and methylene backbone (s–CH_2–), respectively. The ratio of s-CH_3/s–CH_2– in OTT-, DDT-, and HDT-capped Ag_2Se QDs increased with the elongation of chain length, declaring the gradually improved order degree of the ligand anchored on the QDs surface, which was primarily attributed to the stronger interactions between longer aliphatic chains [25, 26]. Thereinto, the stronger hydrophobic chain–chain interaction led to a sparser distribution of ligands on the QD surface and more exposed surface traps, thus damaging the QDs PLQY.

As a result, by understanding the influences of the aliphatic chain length of the ligands on binding affinity and surface states, as well as the order degree of the ligand on the QDs surface, we proposed two possible reasons to explain the distinction in PL intensities originating from different ligands functionalized Ag_2Se QDs: 1) The discrepancy in passivation capability caused by the different surface binding affinity has significant impacts on the surface states and the charge trapping behaviors of QDs, further affecting the PLQY of QDs. 2) The ligand–ligand interaction varied with the aliphatic chain length affected the order degree and conformation of ligands anchoring on the QDs surface, thereafter disturbed the surface states of QDs, and tuned the optical properties of QDs.

3.3 The effect of ligand chain length on the alloyed AgAuSe QDs

Although the PL intensity of Ag_2Se QDs could be significantly enhanced by optimizing the surface ligand to reduce their surface trap states, Ag_2Se QDs capped with OTT ligand failed to exhibit desirable PLQY. Recently, we successfully developed a span-new strategy to obtain AgAuSe QDs with spectacular PLQY by alloying parent Ag_2Se QDs with Au precursor, in which the cation vacancies and crystal defects produced from the high mobility of Ag^+ in Ag_2Se QDs were effectively inhibited by Au^+ species [8]. Therefore, we further investigated the luminescence performance of subsequent AgAuSe QDs by alloying OTT-, DDT-, and HDT-capped Ag_2Se QDs with Au^+, respectively. As exhibited in Figs. 3(a)–3(c), a series of homogeneous AgAuSe QDs with almost identical average sizes of 4.3 nm were prepared via cation exchange method. The energy-dispersive spectroscopy (EDS) mappings (Fig. S11 in the ESM) displayed the successful incorporation of Au in AgAuSe QDs. Additionally, the PXRD patterns (Fig. S12 in the ESM) revealed the broad diffraction peaks of these alloyed AgAuSe QDs, which could be well-indexed to bcc AgAuSe (JCPDS No. 25-0367). Further, the XPS and UPS results indicated the successful alloying of Ag_2Se QDs with Au^+ and the ligand-induce dipole tuned the bandgap positions in the obtained AgAuSe QDs (Figs. S13–S15 in the ESM). Subsequently, the optical properties of these alloyed AgAuSe QDs were studied. As exhibited in Fig. 3(d), the PL spectra presented a notable blue shift from 1,600 to 970 nm, as well the absorption spectra (Fig. S16 in the ESM), which were driven from the widened bandgap. Notably, the alloyed AgAuSe QDs showed a significant enhancement of two orders of magnitude in PL intensity, which also increased with the ligand chain lengths decreased as demonstrated in the case of Ag_2Se QDs. The absolute PLQY of OTT-AgAuSe QDs at 970 nm was measured as a striking record of 87.2% in the NIR-II window (900–1,700 nm) (Fig. 3(e) and Fig. S17 in the ESM) [33–35]. Meanwhile, the PL lifetime τ in Fig. 3(f) was also prolonged from 3.51 to 4.82 μs as the chain-length shortening. Additionally, the calculated radiative recombination rate k_{rad} and nonradiative recombination rate k_{non} of the AgAuSe QDs were shown in Table S1 in the ESM, which manifested OTT-AgAuSe QDs possess the lowest defect density relative to DDT- and HDT-AgAuSe. Furthermore, we verified the success of the chain length induced high PLQY in different sized AgAuSe QDs (Figs. S18 and S19 in the ESM). The OTT-AgAuSe QDs with a size of 5.2 nm

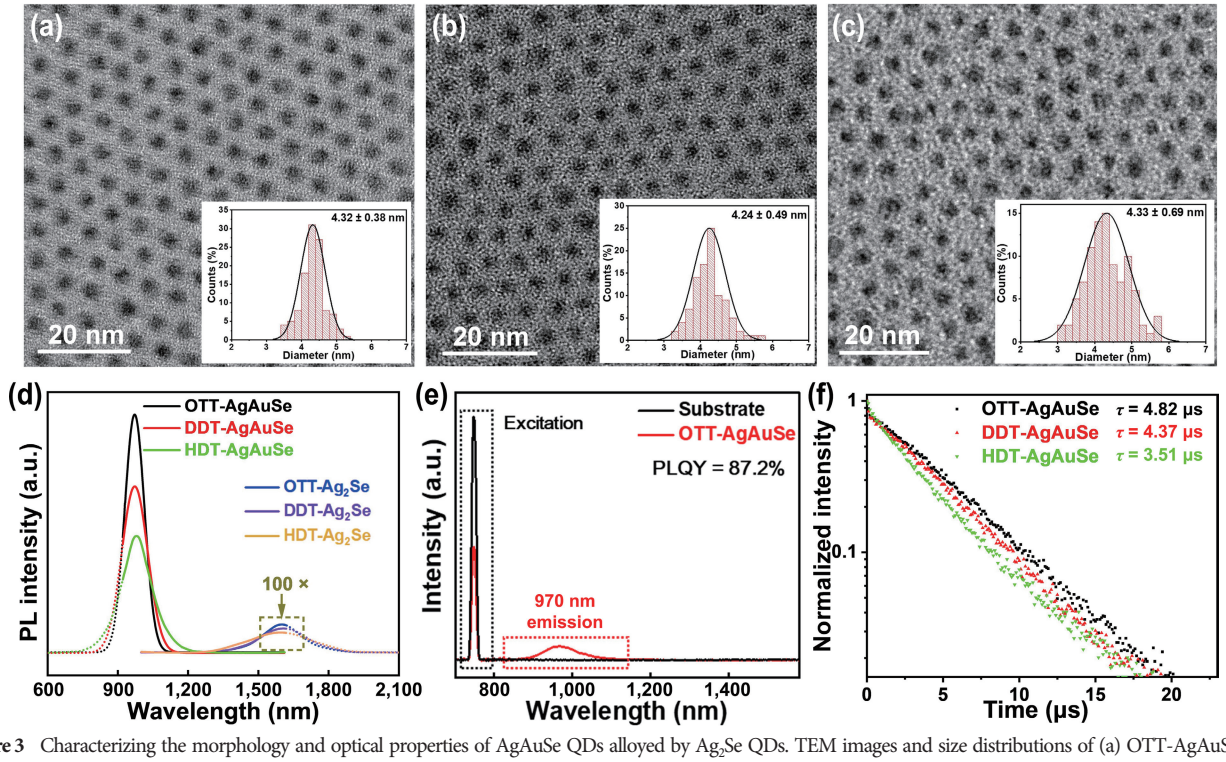

Figure 3 Characterizing the morphology and optical properties of AgAuSe QDs alloyed by Ag_2Se QDs. TEM images and size distributions of (a) OTT-AgAuSe, (b) DDT-AgAuSe, and (c) HDT-AgAuSe QDs. (d) PL spectra of the obtained AgAuSe QDs with emission at 970 nm under the same atomic concentration. (e) Absolute PLQY of OTT-AgAuSe QDs emitted at 970 nm. (f) Time-resolved PL spectra and lifetime of OTT-, DDT-, and HDT-capped AgAuSe QDs emitted at 970 nm. The exciton recombination process was fitted by monoexponential decay function.

exhibited the highest PLQY (86.3%) at the PL emission of 1,045 nm, along with the longest lifetime (5.50 μs), among three samples (Figs. S20–S22 in the ESM). To sum up, in addition to the suppression of the traps in crystal lattice of Ag_2Se by incorporating Au, the significantly improved PLQY and lifetime of OTT-AgAuSe QDs were ascribed to the excellent surface passivation of OTT for Ag_2Se QDs.

3.4 *In vivo* angiography imaging with an ultra-low dosage under an ultra-low excitation intensity

Due to the much-depressed photon absorption and tissue scattering, NIR-II was considered as the optimal window for *in vivo* imaging [36–38]. Considering the extremely high PLQY of the NIR-II-emitting OTT-AgAuSe QDs, DSPE-mPEG-modified AgAuSe QDs with emission at 1,045 nm (Fig. S23 in the ESM) were used to implement *in vivo* imaging under an ultra-low dosage (185 $\mu g \cdot kg^{-1}$) and excitation power density (2 $mW \cdot cm^{-2}$, 808 nm). To evaluate the advantage of the high PLQY AgAuSe QDs in *in vivo* imaging, we benchmarked it against ICG dye, which was the most widely used NIR fluorescent probe in clinical diagnosis [39]. Figure 4(a) showed the optical images of two probes with the same mass concentration (25 $\mu g \cdot mL^{-1}$) along with distilled H_2O (dH_2O). The corresponding fluorescence image in Fig. 4(b) emerged the prominent brightness of PEGylated AgAuSe QDs, albeit its mole concentration was far below that of ICG. After the administration of these two probes (25 $\mu g \cdot mL^{-1}$, 150 μL) via tail intravenous injection into mice respectively, the leg vascular networks of mice injected with AgAuSe QDs were more clearly visualized with higher spatial resolution (Figs. 4(c)–4(f)) and higher signal-to-noise ratio (Fig. S24 in the ESM). It is worthy to note that the administrated dose of AgAuSe QDs (185 $\mu g \cdot kg^{-1}$) and the excitation laser power density (2 $mW \cdot cm^{-2}$, 808 nm) were much lower than other imaging probes reported in the Refs. [40–44], due to its unprecedentedly high PLQY. Such a low dosage and laser power intensity will be of great significance for the potential clinical translation of AgAuSe QDs avoiding the biosafety concerns.

4 Conclusions

In summary, we have investigated the effect of aliphatic chain length on the optical properties of Ag_2Se QDs by selecting OTT, DDT, and HDT as capping ligands. The shortest OTT ligand was found to act as the ideal ligand for synthesizing high-quality Ag_2Se QDs compared to DDT and HDT, originating from its excellent passivation capability for surface defects as illustrated by experimental and theoretical results. Alloying the high-quality of parent OTT-Ag_2Se QDs with Au^+ precursor, nearly trap-free AgAuSe QDs were obtained, possessing a record absolute PLQY of 87.2% with PL emission at 970 nm. Further, by the virtue of its high PLQY in the NIR-II window, PEGylated AgAuSe QDs enable *in vivo* angiography imaging at an ultra-low dosage of 185 $\mu g \cdot kg^{-1}$ by illuminating with an 808 nm laser at an ultra-low power intensity of 2 $mW \cdot cm^{-2}$. We expect that our findings of the roles of the ligand chain length played on the optical properties of QDs could be helpful and suggestive to the design and synthesis of high-quality QDs, and also look forward to the wide applications of AgAuSe QDs with unprecedentedly high brightness in various fields, such as bioimaging, optoelectronic devices, solar cells, etc.

Acknowledgements

This work was financially supported by the National Natural Science Foundation of China (Nos. 21934007 and 22001262), the Strategic Priority Research Program of Chinese Academy of Sciences (No. XDB36000000), the Natural Science Foundation of Jiangsu Province (No. BK20200254), and China Postdoctoral Science Foundation (No. 2019M661966). The authors thank Suzhou NIR-Optics Technologies Co., Ltd. for its instrumental and technical support on the NIR-II imaging.

Electronic Supplementary Material: Supplementary material (the size distributions, XPS, atoms proportion, TGA, UPS, FWHM, absorbance/emission spectra, structure model diagram and ^1H NMR results of Ag_2Se QDs; the EDS mapping, power XRD patterns, XPS, UPS, absorbance/emission spectra, TEM, PLQY, time-resolved PL spectra of AgAuSe QDs, and the SNR

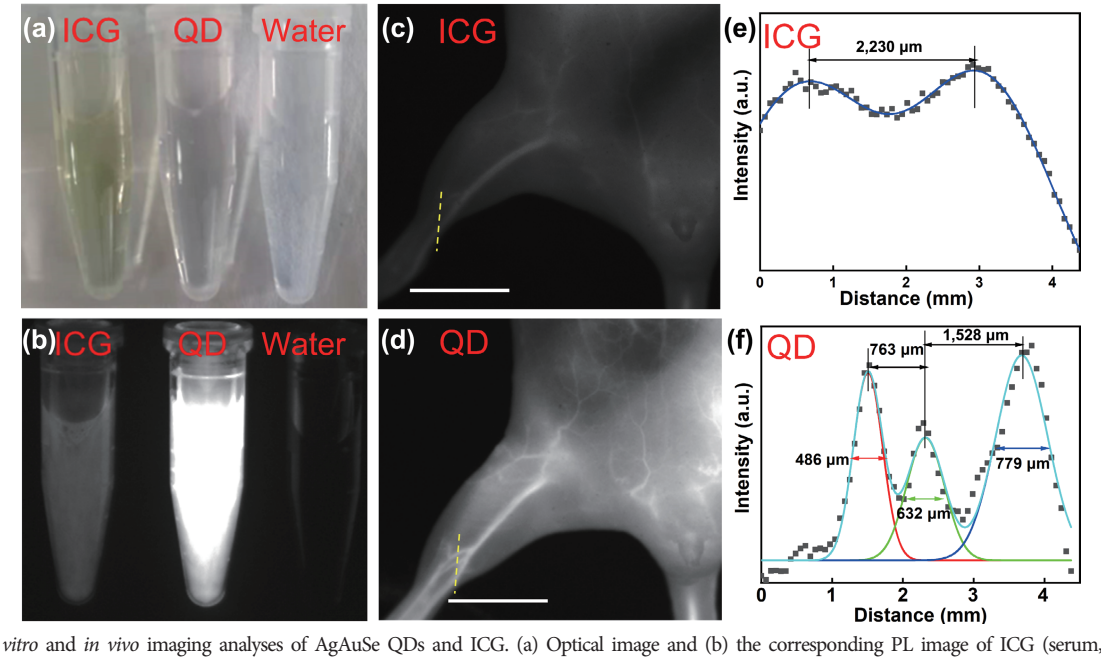

Figure 4 *In vitro* and *in vivo* imaging analyses of AgAuSe QDs and ICG. (a) Optical image and (b) the corresponding PL image of ICG (serum, 25 $\mu g \cdot mL^{-1}$), PEGylated AgAuSe QDs (PBS, 25 $\mu g \cdot mL^{-1}$), and dH_2O excited by an 808 nm laser. ICG was dispersed in serum to avoid aggregation-induced quenching. The 808 nm laser power was 2 $mW \cdot cm^{-2}$ and exposure time was 20 ms. *In vivo* angiography of mice administrated with (c) ICG and (d) AgAuSe QDs upon 808 nm laser excitation (dosage: 185 $\mu g \cdot kg^{-1}$, power intensity: 2 $mW \cdot cm^{-2}$, and exposure time: 300 ms). The scale bar was 1 cm. (e)–(f) Cross-sectional fluorescence intensity profiles of mice injected with ICG and AgAuSe QDs, respectively.

analysis of mice injected with ICG and AgAuSe QDs) is available in the online version of this article at https://doi.org/10.1007/s12274-022-4417-0.

References

[1] Boles, M. A.; Ling, D. S.; Hyeon, T.; Talapin, D. V. The surface science of nanocrystals. *Nat. Mater.* **2016**, *15*, 141–153.

[2] Weiss, E. A. Organic molecules as tools to control the growth, surface structure, and redox activity of colloidal quantum dots. *Acc. Chem. Res.* **2013**, *46*, 2607–2615.

[3] Kirkwood, N.; Monchen, J. O. V.; Crisp, R. W.; Grimaldi, G.; Bergstein, H. A. C.; Du Fossé, I.; Van Der Stam, W.; Infante, I.; Houtepen, A. J. Finding and fixing traps in II-VI and III-V colloidal quantum dots: The importance of *Z*-type ligand passivation. *J. Am. Chem. Soc.* **2018**, *140*, 15712–15723.

[4] Li, Y.; Pu, C. D.; Peng, X. G. Surface activation of colloidal indium phosphide nanocrystals. *Nano Res.* **2017**, *10*, 941–958.

[5] Kumar, S.; Jagielski, J.; Marcato, T.; Solari, S. F.; Shih, C. J. Understanding the ligand effects on photophysical, optical, and electroluminescent characteristics of hybrid lead halide perovskite nanocrystal solids. *J. Phys. Chem. Lett.* **2019**, *10*, 7560–7567.

[6] Battaglia, D.; Peng, X. G. Formation of high quality InP and InAs nanocrystals in a noncoordinating solvent. *Nano Lett.* **2002**, *2*, 1027–1030.

[7] Yu, W. W.; Peng, X. G. Formation of high-quality CdS and other II-VI semiconductor nanocrystals in noncoordinating solvents: Tunable reactivity of monomers. *Angew. Chem., Int. Ed.* **2002**, *41*, 2368–2371.

[8] Yang, H. C.; Li, R. F.; Zhang, Y. J.; Yu, M. X.; Wang, Z.; Liu, X.; You, W. W.; Tu, D. T.; Sun, Z. Q.; Zhang, R. et al. Colloidal alloyed quantum dots with enhanced photoluminescence quantum yield in the NIR-II window. *J. Am. Chem. Soc.* **2021**, *143*, 2601–2607.

[9] Du, Y. P.; Xu, B.; Fu, T.; Cai, M.; Li, F.; Zhang, Y.; Wang, Q. B. Near-infrared photoluminescent Ag_2S quantum dots from a single source precursor. *J. Am. Chem. Soc.* **2010**, *132*, 1470–1471.

[10] Yang, Y.; Qin, H. Y.; Jiang, M. W.; Lin, L.; Fu, T.; Dai, X. L.; Zhang, Z. X.; Niu, Y.; Cao, H. J.; Jin, Y. Z. et al. Entropic ligands for nanocrystals: From unexpected solution properties to outstanding processability. *Nano Lett.* **2016**, *16*, 2133–2138.

[11] Yin, Y. D.; Alivisatos, A. P. Colloidal nanocrystal synthesis and the organic–inorganic interface. *Nature* **2005**, *437*, 664–670.

[12] Krieg, F.; Ochsenbein, S. T.; Yakunin, S.; Ten Brinck, S.; Aellen, P.; Süess, A.; Clerc, B.; Guggisberg, D.; Nazarenko, O.; Shynkarenko, Y. et al. Colloidal $CsPbX_3$ (X = Cl, Br, I) nanocrystals 2.0: Zwitterionic capping ligands for improved durability and stability. *ACS Energy Lett.* **2018**, *3*, 641–646.

[13] Pan, J.; Shang, Y. Q.; Yin, J.; De Bastiani, M.; Peng, W.; Dursun, I.; Sinatra, L.; El-Zohry, A. M.; Hedhili, M. N.; Emwas, A. H. et al. Bidentate ligand-passivated $CsPbI_3$ perovskite nanocrystals for stable near-unity photoluminescence quantum yield and efficient red light-emitting diodes. *J. Am. Chem. Soc.* **2018**, *140*, 562–565.

[14] Zhang, Y.; Li, G. S.; She, C. K.; Liu, S. H.; Yue, F. Y.; Jing, C. B.; Cheng, Y.; Chu, J. H. Room temperature preparation of highly stable cesium lead halide perovskite nanocrystals by ligand modification for white light-emitting diodes. *Nano Res.* **2021**, *14*, 2770–2775.

[15] Owen, J. The coordination chemistry of nanocrystal surfaces. *Science* **2015**, *347*, 615–616.

[16] Houtepen, A. J.; Hens, Z.; Owen, J. S.; Infante, I. On the origin of surface traps in colloidal II-VI semiconductor nanocrystals. *Chem. Mater.* **2017**, *29*, 752–761.

[17] Grisorio, R.; Debellis, D.; Suranna, G. P.; Gigli, G.; Giansante, C. The dynamic organic/inorganic interface of colloidal PbS quantum dots. *Angew. Chem., Int. Ed.* **2016**, *55*, 6628–6633.

[18] Hassinen, A.; Moreels, I.; De Nolf, K.; Smet, P. F.; Martins, J. C.; Hens, Z. Short-chain alcohols strip X-type ligands and quench the luminescence of PbSe and CdSe quantum dots, acetonitrile does not. *J. Am. Chem. Soc.* **2012**, *134*, 20705–20712.

[19] Anderson, N. C.; Hendricks, M. P.; Choi, J. J.; Owen, J. S. Ligand exchange and the stoichiometry of metal chalcogenide nanocrystals: Spectroscopic observation of facile metal-carboxylate displacement and binding. *J. Am. Chem. Soc.* **2013**, *135*, 18536–18548.

[20] Kalyuzhny, G.; Murray, R. W. Ligand effects on optical properties of CdSe nanocrystals. *J. Phys. Chem. B* **2005**, *109*, 7012–7021.

[21] Stein, J. L.; Mader, E. A.; Cossairt, B. M. Luminescent InP quantum dots with tunable emission by post-synthetic modification with Lewis acids. *J. Phys. Chem. Lett.* **2016**, *7*, 1315–1320.

[22] Calvin, J. J.; Swabeck, J. K.; Sedlak, A. B.; Kim, Y.; Jang, E.; Alivisatos, A. P. Thermodynamic investigation of increased luminescence in indium phosphide quantum dots by treatment with metal halide salts. *J. Am. Chem. Soc.* **2020**, *142*, 18897–18906.

[23] Nenon, D. P.; Pressler, K.; Kang, J.; Koscher, B. A.; Olshansky, J. H.; Osowiecki, W. T.; Koc, M. A.; Wang, L. W.; Alivisatos, A. P. Design principles for trap-free $CsPbX_3$ nanocrystals: Enumerating and eliminating surface halide vacancies with softer Lewis bases. *J. Am. Chem. Soc.* **2018**, *140*, 17760–17772.

[24] Balan, A. D.; Olshansky, J. H.; Horowitz, Y.; Han, H. L.; O'Brien, E. A.; Tang, L.; Somorjai, G. A.; Alivisatos, A. P. Unsaturated ligands seed an order to disorder transition in mixed ligand shells of CdSe/CdS quantum dots. *ACS Nano* **2019**, *13*, 13784–13796.

[25] Calvin, J. J.; O'Brien, E. A.; Sedlak, A. B.; Balan, A. D.; Alivisatos, A. P. Thermodynamics of composition dependent ligand exchange on the surfaces of colloidal indium phosphide quantum dots. *ACS Nano* **2021**, *15*, 1407–1420.

[26] Elimelech, O.; Aviv, O.; Oded, M.; Banin, U. A tale of tails: Thermodynamics of CdSe nanocrystal surface ligand exchange. *Nano Lett.* **2020**, *20*, 6396–6403.

[27] Delley, B. From molecules to solids with the $DMol^3$ approach. *J. Chem. Phys.* **2000**, *113*, 7756–7764.

[28] Perdew, J. P.; Burke, K.; Ernzerhof, M. Generalized gradient approximation made simple. *Phys. Rev. Lett.* **1996**, *77*, 3865–3868.

[29] Zhu, C. N.; Jiang, P.; Zhang, Z. L.; Zhu, D. L.; Tian, Z. Q.; Pang, D. W. Ag_2Se quantum dots with tunable emission in the second near-infrared window. *ACS Appl. Mater. Interfaces* **2013**, *5*, 1186–1189.

[30] Pearson, R. G. Absolute electronegativity and hardness: Application to inorganic chemistry. *Inorg. Chem.* **1988**, *27*, 734–740.

[31] Brown, P. R.; Kim, D.; Lunt, R. R.; Zhao, N.; Bawendi, M. G.; Grossman, J. C.; Bulovic, V. Energy level modification in lead sulfide quantum dot thin films through ligand exchange. *ACS Nano* **2014**, *8*, 5863–5872.

[32] Morris-Cohen, A. J.; Vasilenko, V.; Amin, V. A.; Reuter, M. G.; Weiss, E. A. Model for adsorption of ligands to colloidal quantum dots with concentration-dependent surface structure. *ACS Nano* **2012**, *6*, 557–565.

[33] Lian, W.; Tu, D. T.; Hu, P.; Song, X. R.; Gong, Z. L.; Chen, T.; Song, J. B.; Chen, Z.; Chen, X. Y. Broadband excitable NIR-II luminescent nano-bioprobes based on $CuInSe_2$ quantum dots for the detection of circulating tumor cells. *Nano Today* **2020**, *35*, 100943.

[34] Santos, H. D. A.; Gutierrez, I. Z.; Shen, Y. L.; Lifante, J.; Ximendes, E.; Laurenti, M.; Méndez-González, D.; Melle, S.; Calderón, O. G.; Cabarcos, E. L. et al. Ultrafast photochemistry produces superbright short-wave infrared dots for low-dose *in vivo* imaging. *Nat. Commun.* **2020**, *11*, 2933.

[35] Weidman, M. C.; Beck, M. E.; Hoffman, R. S.; Prins, F.; Tisdale, W. A. Monodisperse, air-stable PbS nanocrystals via precursor stoichiometry control. *ACS Nano* **2014**, *8*, 6363–6371.

[36] Li, C. Y.; Wang, Q. B. Challenges and opportunities for intravital near-infrared fluorescence imaging technology in the second transparency window. *ACS Nano* **2018**, *12*, 9654–9659.

[37] Li, C. Y.; Li, F.; Zhang, Y. J.; Zhang, W. J.; Zhang, X. E.; Wang, Q. B. Real-time monitoring surface chemistry-dependent *in vivo* behaviors of protein nanocages via encapsulating an NIR-II Ag_2S quantum dot. *ACS Nano* **2015**, *9*, 12255–12263.

[38] Chen, M.; Feng, S. J.; Yang, Y. M.; Li, Y. X.; Zhang, J.; Chen, S. Y.; Chen, J. Tracking the *in vivo* spatio-temporal patterns of neovascularization via NIR-II fluorescence imaging. *Nano Res.* **2020**, *13*, 3123–3129.

[39] Hu, Z. H.; Fang, C.; Li, B.; Zhang, Z. Y.; Cao, C. G.; Cai, M. S.; Su, S.; Sun, X. W.; Shi, X. J.; Li, C. et al. First-in-human liver-tumour

surgery guided by multispectral fluorescence imaging in the visible and near-infrared-I/II windows. *Nat. Biomed. Eng.* **2020**, *4*, 259–271.

[40] Liu, Z. Y.; Liu, A. A.; Fu, H. H.; Cheng, Q. Y.; Zhang, M. Y.; Pan, M. M.; Liu, L. P.; Luo, M. Y.; Tang, B.; Zhao, W. et al. Breaking through the size control dilemma of silver chalcogenide quantum dots via trialkylphosphine-induced ripening: Leading to Ag_2Te emitting from 950 to 2,100 nm. *J. Am. Chem. Soc.* **2021**, *143*, 12867–12877.

[41] Shi, X. L.; Chen, S.; Luo, M. Y.; Huang, B.; Zhang, G. Z.; Cui, R.; Zhang, M. X. Zn-doping enhances the photoluminescence and stability of PbS quantum dots for *in vivo* high-resolution imaging in the NIR-II window. *Nano Res.* **2020**, *13*, 2239–2245.

[42] Alifu, N.; Zebibula, A.; Zhang, H. Q.; Ni, H. W.; Zhu, L.; Xi, W.; Wang, Y. L.; Zhang, X. L.; Wu, C. F.; Qian, J. NIR-IIb excitable bright polymer dots with deep-red emission for *in vivo* through-skull three-photon fluorescence bioimaging. *Nano Res.* **2020**, *13*, 2632–2640.

[43] Zhong, Y. T.; Ma, Z. R.; Zhu, S. J.; Yue, J. Y.; Zhang, M. X.; Antaris, A. L.; Yuan, J.; Cui, R.; Wan, H.; Zhou, Y. et al. Boosting the down-shifting luminescence of rare-earth nanocrystals for biological imaging beyond 1,500 nm. *Nat. Commun.* **2017**, *8*, 737.

[44] Zhang, X. D.; Wang, H. S.; Antaris, A. L.; Li, L. L.; Diao, S.; Ma, R.; Nguyen, A.; Hong, G. S.; Ma, Z. R.; Wang, J. et al. Traumatic brain injury imaging in the second near-infrared window with a molecular fluorophore. *Adv. Mater.* **2016**, *28*, 6872–6879.